



HAL
open science

Theoretical analysis of flow effects in spatially-encoded diffusion NMR

Rituraj Mishra, Jean-Nicolas Dumez

► **To cite this version:**

Rituraj Mishra, Jean-Nicolas Dumez. Theoretical analysis of flow effects in spatially-encoded diffusion NMR. *The Journal of Chemical Physics*, 2022, 10.1063/5.0130125 . hal-03900072

HAL Id: hal-03900072

<https://hal.science/hal-03900072v1>

Submitted on 15 Dec 2022

HAL is a multi-disciplinary open access archive for the deposit and dissemination of scientific research documents, whether they are published or not. The documents may come from teaching and research institutions in France or abroad, or from public or private research centers.

L'archive ouverte pluridisciplinaire **HAL**, est destinée au dépôt et à la diffusion de documents scientifiques de niveau recherche, publiés ou non, émanant des établissements d'enseignement et de recherche français ou étrangers, des laboratoires publics ou privés.



Distributed under a Creative Commons Attribution - NonCommercial 4.0 International License

Theoretical analysis of flow effects in spatially-encoded diffusion NMR

Rituraj Mishra and Jean-Nicolas Dumez*

Nantes Université, CNRS, CEISAM, UMR6230, F-4400 Nantes, France

ABSTRACT

The measurement of translational diffusion coefficients by nuclear magnetic resonance (NMR) spectroscopy is essential in a broad range of fields including organic, inorganic, polymer and supramolecular chemistry. It is also a powerful method for mixture analysis. Spatially-encoded diffusion (SPEN-D) NMR is a time efficient technique to collect diffusion NMR data, which is particularly relevant for the analysis of samples that evolve in time. In many cases, motion other than diffusion is present in NMR samples. This is for example the case of flow NMR experiments for, e.g., online reaction monitoring, and in the presence of sample convection. Such motion is deleterious for the accuracy of DNMR experiments in general, and for SPEN DNMR in particular. Limited theoretical understanding of flow effects in SPEN DNMR experiments is an obstacle to their broader experimental implementation. Here, we present a detailed theoretical analysis of flow effects in SPEN DNMR, and of their compensation, throughout the relevant pulse sequences. This analysis is validated by comparison with numerical simulation performed with the Fokker-Planck formalism. We then consider, through numerical simulation, the specific cases of constant, laminar and convection flow, and the accuracy of SPEN DNMR experiments in these contexts. This analysis will be useful for the design and implementation of fast diffusion NMR experiments, and for their applications.

* email: jean-nicolas.dumez@univ-nantes.fr

I. INTRODUCTION

Nuclear magnetic resonance spectroscopy is a powerful approach to measure the translational diffusion coefficients of molecules in solution.¹ Diffusion NMR measurements are used to probe polymer sizes,²⁻⁵ to characterise host-guest interactions,⁶⁻⁹ and to measure the size of aggregates,¹⁰⁻¹³ among other things. Diffusion NMR is also widely used as a way to separate the spectral information on components in a mixture, without physical separation of the components themselves. This approach is used for applications ranging from authentication^{14,15} to reaction monitoring.^{16,17}

The measurement of diffusion coefficients by NMR is based on the application of a pair of magnetic field gradient pulses, separated by a delay. Diffusion during the delay results in an attenuation of the NMR signals. Conventional diffusion NMR experiments rely on the stepwise incrementation of the area of the gradient pulses across a series of consecutive scans. This results in experiment duration of a few minutes or more. Spatially Encoded Diffusion NMR (SPEN DNMR) makes it possible to collect a complete data set in a single scan of less than one second, by spatial parallelisation of the gradient pulse area.¹⁸⁻²² In SPEN DNMR pulse sequence, the gradient pulses found in conventional DNMR are replaced by the combined application of a gradient pulse and a frequency swept pulse. This fast DNMR method has proven useful for the monitoring of chemical reactions,²² and for the analysis of hyperpolarised samples.^{23,24}

Diffusion NMR experiments are sensitive to the displacements of molecules, even if they are not due to diffusion. In particular, DNMR experiments are sensitive to any mesoscopic displacements within the sample, and this can result in highly inaccurate estimates of the diffusion coefficients. For example, convection effects, if left uncompensated, are well-known to result in overestimated diffusion coefficients.²⁵⁻²⁸ The accurate measurement of diffusion coefficients for a sample in continuous flow is also particularly challenging.^{17,29} The effect of flow on conventional diffusion NMR and MRI is well studied theoretically and experimentally.³¹⁻⁴⁰ Notably, it can be shown that a constant velocity flow results in an additional phase shift of the magnetization. For conventional experiments, an elegant convection compensation strategy was introduced by Jerschow and Mueller in 1998.⁴¹ It consists of using two diffusion encoding steps

instead of one, designed such that the effect of convection cancels out. This approach has become standard for DNMR experiments carried out in solvents that are prone to convection.^{1,42} It has also been exploited for diffusion measurements in continuous flow.^{17,43}

Convection compensation has also been extended to the case of spatially-encoded diffusion NMR experiments.^{22,24} Following the idea of flow-compensated conventional diffusion sequence, two diffusion encoding blocks are used instead of one. This has led to the possibility to collect accurate DNMR data for samples hyperpolarised with dissolution dynamic nuclear polarisation,²⁴ and also for the real-time monitoring of a chemical reaction in an organic solvent.²² While simplistic numerical simulation and analytical calculations hinted at the validity of this approach,^{24,44} flow effects in SPEN DNMR experiments remain poorly described and understood. This is also an obstacle in using these experiments for reaction monitoring by flow NMR.

In this article, we provide a detailed theoretical description of flow effects in SPEN DNMR experiments, supported by numerical spin simulation. We use the propagator model³³ to derive analytical expressions of the echo amplitude for the SPEN stimulated echo and double stimulated echo pulse sequence. These expressions work outside of the small displacement approximation that was used in earlier work, and are validated by exact numerical simulation using the SPINACH library.^{19,45–47} We also describe flow effects during the acquisition part of SPEN DNMR pulse sequences. This framework is then used to analyse three cases of practical importance, plug flow, laminar flow, and convection flow. In the three cases, the expected accuracy of SPEN DNMR experiments is discussed, and data processing strategies to improve it are described. Overall, this study provides both physical insights and practical tools for applications of SPEN DNMR in the presence of flow, be it for reaction monitoring or the analysis of hyperpolarised samples.

II. NUMERICAL METHODS

A. Numerical simulations for a single velocity

All the numerical simulations were performed with the SPINACH library, version 2.3.4934.^{19,45–47} An ensemble of uncoupled spins $I = 1/2$ was considered, with a translational diffusion coefficient of $8 \times 10^{-10} \text{ m}^2/\text{s}$. The simulated pulse sequences are shown in Fig. 1. Simulations were performed with linearly swept chirp pulses with a duration of 1.5 ms and a bandwidth of 110 kHz. The

encoding gradients had an amplitude of 0.2535 T/m, resulting in a size of 10 mm for the spatial region swept by the pulse. A sample length of 15 mm was equally divided in 3000 spatial grid points. The diffusion delay Δ was set to 150 ms. The effect of relaxation was not considered during the simulation. The unwanted coherences were removed by setting them equal to zero.

1. Without explicit acquisition

In order to characterise the encoding process only, the acquisition block was not simulated, and the transverse component of the magnetisation at the end of the encoding block was obtained as a function of position simply by retaining the corresponding element of the state vector.

The comparison with analytical expressions of the diffusion decay required a reference profile, that was obtained by running the simulation with the translational diffusion coefficient set to 0 m²/s. Experimentally, the reference profile can be obtained by using the minimum possible diffusion delay. While this introduces some additional error (because of diffusion during the spatial encoding block), this error is similar with and without flow effects.

2. With explicit acquisition

When simulated, the acquisition block of the pulse sequence consisted of a train of bipolar gradient pulses of strength ± 0.52 T/m and of duration 2τ for each pulse, preceded by a prephasing gradient pulse of strength -0.52 T/m and of duration τ . Each gradient pulse of duration τ (2τ) is divided into 64 (128) points with the fixed dwell time dw of 1.5×10^{-6} s. The EPSI block is shown in Fig. 1. In the following, the origin of the time axis for acquisition will be at the start of the prephasing gradient pulse, although the data points from 0 to τ are discarded. The segment from $(4q + 1)\tau$ to $(4q + 3)\tau$, with $q \in \mathbb{N}$, will be called as odd echoes while the segment from $(4q + 3)\tau$ to $(4q + 5)\tau$ as even echoes throughout the manuscript. A combination of one odd and even echo gradient create a single loop and 256 such loops were used to acquire the data. The sign of prephasing and the bipolar gradient shown in Fig. 1c and 1d is for odd echo acquisition while for even echo acquisition, the reverse sign is used for both the gradients.

The resulting 1D data was rearranged into two $M \times N$ 2D matrix, one for odd echoes and one for even echoes, where M is the number of points per gradient pulses, and N is the number

of loops. The data was then 2D Fourier transformed to obtain space-frequency domain data. A slice (intensity as a function of z) was extracted at the location of the maximum in the spectral dimension.

A reference profile was obtained by running the simulation for the whole sequence with the translational diffusion coefficient set to $0 \text{ m}^2/\text{s}$. The diffusion decay curve was divided by the reference profile to compensate for the effect of the spatial selectivity of the chirp + gradient block. The diffusion decay curve, after correction by the reference profile, was used to extract the diffusion coefficient via non-linear least square fitting.

When velocity-correction was applied for the detection period, the simulated signal was multiplied element-wise, before 2D FT, by the $M \times N$ matrix $e^{-i2\pi\gamma G_a t_1 (v_z 4n_l \tau)}$, where t_1 is varying from $-\tau$ to τ , n_l varies from 1 to total number of loops, G_a is the strength of acquisition gradient, and v_z is the linear velocity (see section IV.C).

B. Numerical simulations with a velocity distribution

The effect of laminar and convection flow can be modelled by dividing the sample in elements of constant velocity, as illustrated in Fig. 2. For that purpose, a cross section of the NMR tube is divided in n_{cs} (cs in the subscript stands for cross-section) concentric rings of width dr . In the case of convection flow, each ring is further divided into n_ϕ elements. The total simulated data is obtained with a weighted sum of independent 1D simulations, each performed with constant velocity.

1. Laminar flow

For laminar flow, the velocities corresponding to different rings were calculated according to:³⁴

$$v(r) = v_{max} \left(1 - \left(\frac{r}{a} \right)^2 \right) \quad (1)$$

where r is the radial distance, which varies from 0 to a , where a is the radius of the cross-section of the sample, and v_{max} is the maximum velocity at the center of the cross-section.

Simulations were performed for a grid of radial distance, r_i , from 0 to 2.5 mm in 281 equal steps. The SPEN DNMR simulations for flow compensated sequence were performed for all the

velocities with the parameters, chosen in the starting of this section, except the velocity, dwell time (dw) and number the points in a gradient pulse (m_p). The velocity was chosen to be 5 mm/s. The dw was doubled, i.e., 3×10^{-6} s, and m_p was halved, i.e., 64, to decrease the field of view (FOV) without changing the resolution.

The FIDs acquired with even and odd echoes for each velocity are Fourier transformed (FT) along both dimensions separately to provide space-frequency ($z - \omega$) domain data, $I(r)$. Since the velocity $v(r)$ is independent of the angle ϕ , the double weighted summation over variable radius r and angle ϕ becomes a single sum as follows:

$$I_{laminar} = 2\pi \sum_{i=1}^{n_{cs}} \frac{a}{n_{cs}} r_i I(r_i) \quad (2)$$

The same procedure is used to obtain the reference laminar profile, $I_{laminar}^{ref}$, except all the simulations were performed without diffusion. For analysis and display, the profiles are normalised by dividing the profiles by their maxima.

2. Convection flow

In the case of convection flow, the velocities vary as³¹

$$v(r, \phi) = \sum_{n=0}^{\infty} v_n \left(\frac{I_n(kr)}{I_n(ka)} - \frac{J_n(kr)}{J_n(ka)} \right) \cos(n\phi) \quad (3)$$

where J_n and I_n are Bessel and modified Bessel functions, n is the mode of flow, v_n is a system dependent scalar of velocity for each mode of flow and is non-zero only for odd n and zero for even n , ϕ is varied from 0 to 2π , kr and ka is defined respectively as $R_a^{1/4} \left(\frac{r}{a} \right)$ and $R_a^{1/4}$. The Rayleigh number R_a is given by³¹

$$R_a = - \frac{\beta \rho^2 a^4 c_p g \frac{dT}{dZ}}{\eta \kappa} \quad (4)$$

where β is the volumetric thermal expansion coefficient, ρ is the fluid density, c_p is the specific heat capacity, g is the acceleration due to gravity, $\frac{dT}{dZ}$ is temperature gradient, η is the dynamic viscosity, and κ is the thermal conductivity. In the present article R_a is taken to be 100.

The velocities were varied according Eq. 3 by incrementing the radial distance r sequentially from 0 to 2.5 mm (a) in the steps of $dr = a/n_{cs}$, where $n_{cs} = 26$. The angle ϕ was also sequentially varied from 0 to 2π , in the steps of $d\phi = 2\pi/n_\phi$, where $n_\phi = 25$. Since for NMR experiments only vertical flow is observed therefore $n = 1$ and v_1 was chosen to be 1.5 mm/s. The v_1 is not the maximum velocity unlike in the case of laminar flow. These values result into a $n_\phi \times n_{cs}$ (25×26) velocity profile shown in Fig. 3. Since the profile was symmetrical with respect to $x - z$ plane, only $13 \times 26 = 338$ velocities were chosen to perform the simulation for the flow compensated SPEN DNMR sequence. Except for the value of v_1 , all other parameters are the same as in laminar flow.

The $k - t$ domain fids obtained after the simulation are Fourier transformed in both dimensions to result into (64×256) space-frequency ($z - \omega$) domain data, $I(r_i, \phi_j)$ for each velocity. The final diffusion decay profile for the sample undergoing convection is obtained by weighted summation of $I(r, \phi)$ over the radius r , angle ϕ .

$$I_{convection} = \sum_{j=1}^{n_\phi} \frac{2\pi}{n_\phi} \sum_{i=1}^{n_{cs}} \frac{a}{n_{cs}} r_i I(r_i, \phi_j) \quad (5)$$

By performing the simulation with zero diffusion coefficient, however following the same procedure described above, the reference profile $I_{convection}^{ref}$ is obtained. The diffusion decay curve and reference profiles were extracted from $I_{convection}$ and $I_{convection}^{ref}$. For analysis and display, the profiles are normalised by dividing them by their maxima.

III. SPEN DNMR WITHOUT FLOW

Prior to introducing the effect of flow in spatially encoded diffusion NMR pulse sequences, in this section we will be introducing the SPEN STimulated Echo (STE) pulse sequence, used to acquire diffusion-NMR data, and the general analytical expression used for data analysis.¹⁸⁻²¹ In this study, we rely on a description of diffusion NMR experiments in which magnetisation vectors are used to describe the spins of individual atoms in molecules, which undergo random Brownian motion. This common representation gives correct results for mesoscopic quantities. Note, however, that the numerical simulation in SPINACH instead describes the magnetisation of mesoscopic volume

elements. Molecular motion is not explicitly described, and its effect is accounted for by magnetisation passing between volume elements. The two descriptions are complementary.

A. Diffusion attenuation: qualitative description

Consider first a conventional spin echo sequence, shown in Fig. 1a.¹ The equilibrium magnetisation is first rotated to the transverse plane by the first $\pi/2$ pulse. The first gradient pulse then results in a linear variation of the spin's phase as a function of position, which corresponds to a magnetisation helix. Brownian motion during the diffusion delay then results in partial scrambling of the helix. The second magnetic field gradient pulse then refocuses the magnetisation helix. However, the refocusing is imperfect, because the molecules' positions have changed between the two gradient pulses. As a result, signal acquired after the gradient pair will be attenuated compared to the signal that would be acquired without gradients pulses, to an extent that depends on the pitch of the magnetisation helix, and thus on the area of the gradient pulses. Quantitatively, this attenuation is given by:⁴⁸

$$S = S_0 e^{-\gamma^2 g^2 \delta^2 D \Delta'} \quad (6)$$

where S_0 is the amplitude in the absence of diffusion attenuation, γ is gyromagnetic ratio of the nuclei, g is the gradient strength, δ is the gradient duration, D is the diffusion coefficient, and Δ' is the diffusion delay, corrected to account for the finite width of the gradient pulse (for example, $\Delta' = \Delta - \delta - \delta/3$ in the classic stimulated echo pulse sequence).

This description applies similarly to the conventional stimulated echo pulse sequence, shown in Fig. 1b. The second and first $\pi/2$ pulses in that case serve to store magnetisation along the z axis, to mitigate the effects of relaxation and J modulation, but they have no effect on the diffusion encoding process (the information is temporarily transferred from the spin's phase to their amplitude).

Consider now the SPEN STE DNMR pulse sequence shown in Fig. 1c.¹⁸⁻²¹ The hard $\pi/2$ pulses play the same role as in the conventional sequence. The gradient pulses are replaced by the combined application of a frequency-swept pulse and a gradient pulse. The result of this spatial encoding block is that the effective duration of the gradient pulse experienced by the spins

depends on their position in the sample. Considering also the gradient pulse applied after the chirp pulse, the effective duration of the total gradient pulse varies from 0 at one end of the swept region to $2T_e$ at the other end. This results in a quadratic dependence of the magnetisation's phase with respect to position. Pictorially, this corresponds to a magnetisation helix with a pitch that varies across the sample. Brownian motion during the diffusion delay does, as in the conventional experiment, scramble the helix. And, as in the conventional experiment, the perfect refocusing of the magnetisation, that would be achieved by the second chirp + gradient block in the absence of diffusion, is compromised by molecular motion. The key feature of the SPEN DNMR experiment is that the effect of diffusion is now position dependent. In the absence of flow, the signal acquired for a slice at position z (with a slice width such that the phase variation is approximately linear within the slice), is given by a generalised form of Eq. 6 :⁴⁹

$$S = S_0 e^{-(K(z))^2 D \Delta'} \quad (7)$$

where D is the diffusion coefficient, Δ' is the effective diffusion delay, and $K(z)$ is the spatial derivative of the spin's phase $\phi_{SPEN}(z)$ at the end of the first chirp + gradient block:⁵⁰

$$K(z) = \frac{\partial \phi_{SPEN}(z)}{\partial z} \quad (8)$$

Equation 7 can be derived in several ways. Here we will use the propagator model, which provides a convenient way to then include flow effects.

B. Diffusion attenuation with the propagator model

Assuming that gradient pulses are sufficiently short for the effect of diffusion during the pulses to be negligible (the "narrow-pulse approximation"), the echo amplitude for a pair of identical gradient pulses separated by a delay Δ is given by³³

$$E = \int \bar{P}_s(Z, \Delta) e^{i\phi(Z)} dZ \quad (9)$$

where Z is the dynamic displacement in the gradient direction, $\phi(Z)$ is the spin phase at the end of the second gradient pulse for a molecule displaced by Z , and $\bar{P}_s(Z, \Delta)$ is the average probability that molecules are displaced by Z in time Δ . If translational diffusion is the only motion, then this propagator is given by:³³

$$\bar{P}_s(Z, \Delta) = (4\pi D \Delta)^{-1/2} e^{-Z^2/4D\Delta} \quad (10)$$

In order to calculate the attenuation for a given pulse sequence, one needs to calculate the term $\phi(Z)$. Since the pulse sequence is designed as an echo sequence, the contribution of chemical shift evolution to the phase will not be included during the phase calculation.

The spin phase after the first chirp + gradient block of the SPEN STE pulse sequence can be calculated by assuming that spins flip instantaneously when their resonance frequency matches that of the swept pulse. With this assumption, one has:⁴⁹

$$\phi_{SPEN}(Z) = -\frac{\gamma^2 G_e^2}{R} Z^2 - \gamma G_e T_e Z \quad (11)$$

For the SPEN STE pulse sequence, the phase ϕ_{STE} at the end of the second chirp + gradient block is thus

$$\phi_{STE}(z, z_0) = -\frac{\gamma^2 G_e^2}{R} z^2 - \gamma G_e T_e z + \frac{\gamma^2 G_e^2}{R} z_0^2 + \gamma G_e T_e z_0 \quad (12)$$

where z_0 and z are the position of the molecule at the time of the first and second gradient pulse. Eq. 12 may be rearranged as:

$$\phi_{STE}(z, z_0) = -\gamma G_e T_e (z - z_0) \left(1 + \frac{\gamma G_e}{R T_e} (z_0 + z) \right) \quad (13)$$

Introducing the dynamic displacement, $Z = z - z_0$, one has:

$$\phi_{STE}(Z) = -\gamma G_e T_e Z \left(1 + \frac{\gamma G_e}{R T_e} (2z - Z) \right) \quad (14)$$

$$\phi_{STE}(Z) = -\gamma G_e T_e Z \left(1 + 2 \frac{\gamma G_e}{R T_e} z \right) + \frac{\gamma^2 G_e^2}{R} Z^2 \quad (15)$$

For translational diffusion alone, the mean squared displacement is given by $2D\Delta$, and the last term on the right-hand side of Eq. 15 is negligible provided that

$$2D\Delta \ll \frac{\pi R}{\gamma^2 G_e^2} \quad (16)$$

This condition means that the diffusion length is much smaller than the length of the spatial region over which the phase variation can be considered to be linear.⁵⁰ This quantity will be referred to as the encoding slice width. This condition is usually verified, giving:

$$\phi_{STE}(Z) \approx -\gamma G_e T_e Z \left(1 + 2 \frac{\gamma G_e Z}{RT_e} \right) \quad (17)$$

The approximation of neglecting the squared dynamic displacement in the phase calculation will be referred to as the small-displacement approximation. Equation 17 can be rewritten by identifying the spatial derivative of the spin's phase at the end of the chirp + gradient block:

$$\phi_{STE}(Z) \approx K(z)Z \quad (18)$$

The echo amplitude calculated from Eqs. 9, 10 and 18 provides, after some algebra, the required diffusion-decay equation:

$$E_{STE}^D(z) = e^{-(K(z))^2 D \Delta} \quad (19)$$

C. Echo planar spectroscopic imaging

The spatial-spectral information embedded in the diffusion decay curve obtained after the SPEN STE sequence is unravelled by a train of bipolar gradient pulses, preceded by a prephasing gradient pulse. This acquisition block is known as echo planar spectroscopic imaging (EPSI). In Fig. 1c and Fig. 1d, EPSI blocks are shown as the final step of the pulse sequences. The phase acquired by the magnetization during the EPSI block is given by

$$\phi_{acq}(t) = -\gamma \left(\int_0^t dt' G(t') \right) z \quad (20)$$

where $G(t')$ is the variable acquisition gradient strength (which is $+G_a$ for positive pulses and $-G_a$ for negative pulses). Fig. 4a shows the result of a numerical simulation of an EPSI block, together with the analytical expression given by Eq. 20. The phase during acquisition varies linearly with positive and negative slopes respectively for positive and negative gradients. Further, the phase refocuses at the middle of the odd echo (positive gradient), and even echo (negative gradient).

Data processing and acquisition in MRI is conveniently described by introducing the variable $k(t) = -\gamma \int_0^t dt' G(t')$. The EPSI block results in a zig-zag trajectory in a 2D $k - t$ space. The data from the prephasing gradient is discarded (or simply not acquired). The data from the odd echoes forms a 2D matrix that can be Fourier transformed to give a spectroscopic image. The data from even echoes is processed similarly. The two can be co-added when they give comparable results, which is the case in the absence of flow. The spectroscopic data is then used to extract the diffusion coefficient via least square fitting method with the model Eq. 19 or more precisely Eq. 7.

IV. VELOCITY EFFECTS IN SPEN DNMR

Conventional diffusion NMR pulse sequences are sensitive to flow effects. When molecules move with constant velocity v_z during a stimulated echo pulse sequence, spins acquire an additional phase variation that is proportional to v_z and to the diffusion delay. Similarly, flow also imparts an additional phase to the spins, and to the signal, in SPEN STE pulse sequences. It has been shown, as in the case of conventional diffusion NMR pulse sequences, that the use of two diffusion-encoding steps instead of one makes it possible to refocus the velocity-induced phase^{51,52}. For example, the SPEN double stimulated echo pulse (DSTE) pulse sequence, shown in Fig. 1d, was used for experiments in low-viscosity organic solvents.^{22,24} It consists of two consecutive SPEN STE blocks separated by a π pulse. In this section we will be calculating analytically velocity effects in SPEN DNMR pulse sequence, using the propagator model.

A. Simplified calculation of velocity effects

The effect of a molecular displacement with constant velocity v_z during the diffusion delay of a STE pulse sequence can be taken into account in the propagator model by modifying the propagator as:

$$\bar{P}_s(Z, \Delta) = (4\pi D \Delta)^{-1/2} e^{-(Z - v_z \Delta)^2 / 4D \Delta} \quad (21)$$

The distribution of dynamic displacements is now centred on $v_z \Delta$. The echo amplitude for the SPEN STE block can then still be calculated according to Eq. 9. Let us assume first that the small displacement approximation is fully valid. This gives:

$$E_{STE,a}^{D,v}(z) = e^{-(K(z))^2 D \Delta} e^{iK(z)v_z \Delta} \quad (22)$$

The superscript refers to the fact that both diffusion and velocity effects are taken into account, while the subscript a refers to the fact that an approximate expression of the spin's phase was used.

Consider now the SPEN DSTE pulse sequence. The spin's phase at the end of the final chirp + gradient block is:

$$\phi_{DSTE}(z, z_0, z_1) = -\gamma G_e T_e (z_1 - z) \left(1 + \frac{\gamma G_e}{RT_e} (z + z_1) \right) + \gamma G_e T_e (z - z_0) \left(1 + \frac{\gamma G_e}{RT_e} (z_0 + z) \right) \quad (23)$$

where z_0 , z , and z_1 are the position at the time of the first, second, and fourth chirp + gradient block (the spin's position is assumed to be unchanged between the second and third blocks). Equation 23 may be rewritten by introducing the dynamic displacements $Z = z - z_0$, and $Z' = z_1 - z$ during the first and second diffusion encoding blocks:

$$\phi_{DSTE}(Z, Z') = -\gamma G_e T_e Z' \left(1 + \frac{\gamma G_e}{RT_e} 2z \right) + \frac{\gamma^2 G_e^2}{R} Z'^2 + \gamma G_e T_e Z \left(1 + \frac{\gamma G_e}{RT_e} 2z \right) - \frac{\gamma^2 G_e^2}{R} Z^2 \quad (24)$$

Assuming that the small-displacement approximation is valid:

$$\phi_{DSTE}(Z, Z') \approx -\gamma G_e T_e Z' \left(1 + \frac{\gamma G_e}{RT_e} 2z \right) + \gamma G_e T_e Z \left(1 + \frac{\gamma G_e}{RT_e} 2z \right) \quad (25)$$

Identifying $K(z)$, Eq. 25 can be written:

$$\phi_{DSTE}(Z, Z') \approx K(z) Z' - K(z) Z \quad (26)$$

Substituting the value of phase from Eq. 26 and the average probability factor $\bar{P}_s(Z, \Delta)$ from Eq. 21 in Eq. 9 results into the echo amplitude after the final chirp + gradient block of the SPEN DSTE pulse sequence:

$$E_{DSTE,a}^{D,v}(z) = e^{-2(K(z))^2 D \Delta} \quad (27)$$

The above analytical expression shows that the phase factor, $e^{iK(z)v_z \Delta}$, appeared during the first stimulated echo due to flow is compensated after a π pulse and second stimulated echo.

Numerical simulations provide a powerful mean to test the validity of analytical expressions and of the underlying approximations. Fig. 5 and Fig. 6 show a comparison between the calculated echo amplitude and phase for the SPEN STE and DSTE pulse sequences, given by Eqs 22 and 27, and the result of a numerical simulation of these pulse sequence. Both the magnitude and the phase of the transverse magnetisation are shown. Note that the result of Eq. 22 and 27 is multiplied for that comparison by the reference profile obtained by numerical simulation in the absence of diffusion (see section II), since the analytical calculation does not account for the spatial selectivity of the chirp pulse.

It can be seen that the linear phase observed for the STE sequence in the presence of flow is suppressed for the DSTE sequence. However, while there is good agreement between analytical calculation and numerical simulation of the magnitude in the absence of flow, there is a clear difference between the calculated and the simulated results in the presence of flow. In fact, when the simulated data is fitted according to Eq. 27, a value of $5.06(\pm 0.06) \times 10^{-10} \text{ m}^2/\text{s}$ is obtained in the presence of flow, against $7.95(\pm 0.00) \times 10^{-10} \text{ m}^2/\text{s}$ in the absence of flow.

The discrepancy between numerical simulations and analytical calculation can be traced back to the validity of the small-displacement approximation. While it is always valid in the case of diffusion alone, it is not necessarily the case when flow is present as well. For example, with a velocity of 0.01 m/s and a diffusion delay of 150 ms, molecules move by 1.5 mm between two gradient pulses.

B. Diffusion attenuation and convection compensation, full calculation

In order to separate the effect of diffusion and flow in the calculation of the echo amplitude, it is helpful to make the change of variables

$$Z \leftarrow Z + v_z \Delta \quad (28)$$

in Eq. 9. With this replacement, the propagator, Eq. 21, accounts for diffusion only and becomes equivalent to the propagator shown in Eq. 9, while the phase shift becomes, in the STE case:

$$\phi_{STE} = k(z)(Z + v_z \Delta) + (Z + v_z \Delta)^2 \frac{\gamma^2 G_e^2 T_e}{2\pi BW} \quad (29)$$

The small-displacement approximation remains valid for diffusion, meaning that terms including Z^2 can be neglected. This gives:

$$\phi_{STE} = \left(k(z) + 2v_z\Delta \frac{\gamma^2 G_e^2 T_e}{2\pi BW} \right) Z + k(z)v_z\Delta + v_z^2\Delta^2 \frac{\gamma^2 G_e^2 T_e}{2\pi BW} \quad (30)$$

Combining Eq. 9, 10, and 30 gives, after some algebra:

$$E_{STE}^{D,v}(z) \simeq e^{-\left((k(z))^2 D\Delta + \frac{4v_z^2\Delta^2\gamma^4 G_e^4 T_e^2}{(2\pi BW)^2} D\Delta + 4k(z)v_z\Delta \frac{\gamma^2 G_e^2 T_e}{2\pi BW} D\Delta \right)} e^{ik(z)v_z\Delta} e^{i\left(v_z^2\Delta^2 \frac{\gamma^2 G_e^2 T_e}{2\pi BW} \right)} \quad (31)$$

For typical values of the linear velocity, the argument of the complex exponential in Eq. 31 is negligibly small, such that:

$$E_{STE}^{D,v}(z) \approx e^{-\left((k(z))^2 D\Delta + \frac{4v_z^2\Delta^2\gamma^4 G_e^4 T_e^2}{(2\pi BW)^2} D\Delta + 4k(z)v_z\Delta \frac{\gamma^2 G_e^2 T_e}{2\pi BW} D\Delta \right)} e^{ik(z)v_z\Delta} \quad (32)$$

Defining the encoding slice width as $l_e = \frac{2\pi R}{\gamma^2 G_e^2}$, where $R = \frac{BW}{T_e}$, and root mean square displacement (diffusion length) as $\lambda = \sqrt{2D\Delta}$, this equation becomes

$$E_{STE}^{D,v}(z) \approx e^{-k(z)^2 D\Delta} e^{ik(z)v_z\Delta} e^{-2k(z)v_z\Delta \frac{\lambda^2}{l_e}} e^{-2v_z^2\Delta^2 \left(\frac{\lambda}{l_e} \right)^2} \quad (33)$$

Fig. 5a shows a comparison between the simulated diffusion decay, and the analytical calculation according to Eq. 33. In this case, the simulated and calculated curves are in very good agreement. The small-displacement approximation can be invalid for the flow contribution, in which case the full expression given by Eq. 33 should be used. The small-displacement approximation remains valid for the diffusion contribution. This is consistent with the fact the displacement due to velocity is larger than the encoding slice width, while that due to diffusion is not.

It is interesting to compare the expression of the echo amplitude obtained with (Eq. 22) and without (Eq. 33) making the small-displacement approximation for the flow contribution. Out of the two extra exponential term, the second one is close to one, while the first one has a noticeable role. In fact, if a simulated decay is fitted with Eq. 33, then a diffusion coefficient of $7.77(\pm 0.00) \times 10^{-10} \text{ m}^2/\text{s}$ is obtained (against $5.39(\pm 0.01) \times 10^{-10} \text{ m}^2/\text{s}$ using Eq. 22).

A similar calculation can be performed in the DSTE case. Here we simply report the result that is obtained by making the small-displacement approximation for diffusion only:

$$E_{DSTE}^{D,v}(z) \approx e^{-2D\Delta k(z)^2} e^{-4k(z)v_z\Delta\frac{\lambda^2}{l_e}} e^{-8v_z^2\Delta^2\left(\frac{\lambda}{l_e}\right)^2} \quad (34)$$

Fig. 5b shows a comparison between simulated diffusion decay and analytical expression for DSTE, and the two are in excellent agreement.

Several points can be noted from a comparison of Eqs 27, 33 and 34. First, one can see that, in analogy with the conventional case, double diffusion encoding for SPEN DNMR makes it possible to refocus velocity induced phase variations. However, double diffusion encoding does not compensate for the fact that the position of the encoded region changes between the beginning and the end of each diffusion delay. The use of Eq. 34 for data analysis still makes it possible to retrieve the correct value of the diffusion coefficient, provided that the velocity is known. This will be further discussed below.

C. EPSI: velocity compensation and motion correction

In order to analyse the effect of flow during EPSI, the effect of a constant velocity term on the gradient phase was calculated by replacing z by $z_0 + v_z t'$, where z_0 is the initial position at the time $t = 0$, in Eq. 20.³⁴ The resulting phase during acquisition will hence be given by

$$\phi_{acq}^v(t) = -\gamma \int_0^t dt' G(t')(z_0 + v_z t') \quad (35)$$

where $G(t')$ is variable acquisition gradient strength and is $+G_a$ for positive pulse and $-G_a$ for negative pulses. While the phase gets refocused at the middle of odd and even echo in absence of flow, (Fig. 4a) the phase in presence of flow only refocuses at the middle of even echoes. It can be shown if we calculate the total phase accumulated at 4τ ,^{34,40}

$$\begin{aligned} \phi_{acq}^{wf}(t = 4\tau) = & -\gamma \int_0^\tau dt' (-G_a)(z_0 + v_z t') - \gamma \int_\tau^{2\tau} dt' (G_a)(z_0 + v_z t') - \gamma \int_{2\tau}^{3\tau} dt' (G_a)(z_0 + \\ & v_z t') - \gamma \int_{3\tau}^{4\tau} dt' (-G_a)(z_0 + v_z t') \end{aligned}$$

$$\begin{aligned}
&= +\gamma G_a \left(z_0 \tau + v_z \frac{\tau^2}{2} \right) - \gamma G_a \left(z_0 (2\tau - \tau) + v_z \frac{4\tau^2 - \tau^2}{2} \right) - \gamma G_a \left(z_0 (3\tau - 2\tau) + \right. \\
&v_z \frac{9\tau^2 - 4\tau^2}{2} \left. \right) + \gamma G_a \left(z_0 (4\tau - 3\tau) + v_z \frac{16\tau^2 - 9\tau^2}{2} \right) = 0
\end{aligned} \tag{36}$$

This means that under flow condition, the data from even echoes should be more reliable.

The expression obtained from Eq. 35 can be validated with the result of numerical simulations. The phase of a magnetisation vector at a given position can be obtained from the density matrix as a function of time. Since the velocity induced dephasing is position independent, the comparison can be made for any position in the sample. Fig. 4b shows a comparison between analytical and simulated phases during EPSI for a slice at $z = 4.5$ mm, for the first loop. The two are in perfect agreement.

Using data from even echoes ensures that the magnetisation is suitably refocused at the middle of the gradient pulse even with non-zero velocity. This does not, however, address the fact that the position of the encoded region changes during acquisition. With the parameters used for the simulation (dwell time = 1.5×10^{-6} s, number of loops = 256, number of points in odd/even echo = 128, velocity (v_z) = 0.01 m/s), the position varies in the range of few μm to 1 mm, it results in shifting of magnetisation along the spatial axis. This effect is most easily observed by comparing the Fourier transform of the first and last acquired echoes, for a SPEN DNMR pulse sequence, shown in Fig. 7. If uncorrected, this displacement will introduce an error for the estimated diffusion coefficient.

This effect can also be described by considering the phase of the magnetisation throughout the echo train. The phase during the n_l^{th} even echo can be written as:

$$\phi_{acq}^v(t) = \gamma G_a t_1 \left(z_0 + v_z \frac{(t_1 + 8n_l \tau)}{2} \right) \tag{37}$$

where t_1 is varying from $-\tau$ to τ . Correction by this additional phase in k -dimension will result into linear shift in density matrices along the z -dimension. The overall density matrix in $k - t$ dimension can be obtained by

$$\rho = \int \rho(z) e^{i2\pi \phi_{acq}^v(t)} dz$$

$$\rho = \int \rho(z) e^{+i2\pi\gamma G_a t_1 z_0} e^{+i2\pi\gamma G_a t_1 \left(v_z \frac{t_1}{2} \right)} e^{+i2\pi\gamma G_a t_1 (v_z 4n_l \tau)} dz \quad (38)$$

Since the factor $e^{+i2\pi\gamma G_a t_1 \left(v_z \frac{t_1}{2} \right)} \approx 1$ with the chosen parameters, i.e., $v_z = 0.01 \text{ m/s}$, $t_1 = -64 \times 1.5 \times 10^{-6}$ to $64 \times 1.5 \times 10^{-6}$, therefore

$$\rho = \int \rho(z) e^{i2\pi\gamma G_a t_1 z_0} e^{i2\pi\gamma G_a t_1 (v_z 4n_l \tau)} dz \quad (39)$$

On multiplying the $k - t$ space data by $e^{-i2\pi\gamma G_a t_1 (v_z 4n_l \tau)}$ to remove the effect of additional phase results into a non-sheared $z - \omega$ space data, as shown in Fig. 6b.

V. FLOW SIMULATIONS

Having clear understanding of flow effects during the encoding and acquisition part, the effect of different kinds of flow distributions on SPEN DNMR sequences can be studied. The constant/plug flow corresponds to the simplest situation, the other two most often encountered flow in NMR are laminar flow³⁴ and convection flow.³² In the further section we will discuss these three kinds of flows in the context of SPEN D-NMR.

A. Plug flow

The first case of interest is that of plug flow, that is, motion with a single and uniform velocity. This case was also studied with simulation in Ref.²⁴ Fig. 8 shows the result of the complete simulation of a SPEN DSTE pulse sequence. In panel 8a and 8b, the simulated data was processed without velocity correction, and fitted with Eq. 34 (which accounts for velocity effects). It can be seen that the resulting diffusion coefficient, $6.27 (\pm 0.14) \times 10^{-10} \text{ m}^2/\text{s}$, is under-estimated by 14 %. In contrast, when the data is processed with velocity correction, the estimated diffusion coefficient is $7.90 (\pm 0.01) \times 10^{-10} \text{ m}^2/\text{s}$, which is much closer to the correct value, as shown in panels 8c and 8d. Overall, in order to obtain the correct value of the diffusion coefficients, the effects of flow have to be accounted for during both encoding and detection, and this requires knowledge of the value of the linear velocity. The SPEN DSTE sequence, using even echoes, makes it possible to avoid velocity induced dephasing, but not distortions of the spatial profile. Note that, even if it is not a priori known, the velocity may be measured by NMR, using, for example, a spin-echo based sequence. In principle it may even be possible to obtain the velocity from the phase difference between the centre points of even and odd echoes in the EPSI data. This can be

achieved for the present simulated data, but in practice it would be susceptible to errors due to, e.g. chemical shift evolution.

These results may be compared with those of Ref. ²⁴, which also considered a double-diffusion encoding pulse sequence. In that work, however, flow was only included during the diffusion delays, and not during detection, for the simulations. The observed error, of about 12 %, was then due to the fact that Eq. 19 was used for the fit, which does not account for velocity effects.

Interestingly, as shown in Fig. 9, when velocity effects are not accounted for in the analysis, the fitted diffusion coefficient varies linearly with the input coefficient. The separation power of the experiments would thus still be preserved to some extent. It can be noted, however, that the associated error bar is larger when velocity is not accounted for, because the data is not suitably described by the model. The agreement between fitted and input values is conserved in the presence of noise. By introducing varying levels of noise in the data, it was observed that the estimated uncertainty remains lower than 0.01 m²/s as long as signal-to-noise ratio (S/N) remain ≥ 100 .

B. Laminar flow

Laminar flow is the side-by-side movement of layers of liquid along the direction of flow. The layer near to the surface moves with the minimum velocity mostly due to friction with the surface, however, the layers away from the surface move with higher velocity and reaches a maximum velocity at the centre of the cylinder. The velocity varies from 0 at the edge to v_{max} in the centre, and has mean value $\int_0^a r dr v_z / \int_0^a r dr = v_{max}/2$. Since the velocity in each layer is assumed to be constant, the profile obtained with SPEN DNMR in the case of laminar flow can be modelled as a weightage average of the various constant velocity profiles, as discussed in section II.A.

The profile in the case of laminar flow, $I_{laminar}$ and the corresponding reference profile $I_{laminar}^{ref}$ (obtained with zero diffusion coefficient), are used as input for analysis. In this case, the correction for velocity effects during EPSI, described in section IV.C, cannot be performed. Attempts to perform this correction using the mean velocity were unsuccessful. This is unsurprising, since the average of profiles that are shifted by different amounts is not expected

to be the same as a single profile shifted by the mean displacement. This means that motion during detection can limit the accuracy of SPEN DNMR experiments carried out on a sample that experience laminar flow.

The simulated data in the case of even echoes is shown in Fig. 10a. When this data is fitted with Eq. 34, using the mean velocity, to extract the diffusion coefficient, a value of $6.45(\pm 0.04) \times 10^{-10} \text{ m}^2/\text{s}$ is obtained for the diffusion coefficient. This result is consistent with the plug flow case where the additional velocity correction was not performed and the diffusion coefficient was found to be $6.27(\pm 0.14) \times 10^{-10} \text{ m}^2/\text{s}$. Note that a value of $5.87(\pm 0.06) \times 10^{-10} \text{ m}^2/\text{s}$ is obtained with Eq. 27 is used for the fit, illustrating the fact that the error is reduced when velocity-effects during encoding are accounted for.

The data acquired for the odd echoes was also processed through the same procedure discussed above and had resulted into $5.97(\pm 0.07) \times 10^{-10} \text{ m}^2/\text{s}$ diffusion coefficient which is further from the simulated value. The diffusion decay curve with reference profile and the fitted curve have been shown in Fig. 10. The less accurate diffusion coefficient while processing with odd echoes further testifies the processing of even echo acquired data for the extraction of diffusion coefficient.

Overall, this means that convection compensated SPEN DNMR sequences should be able to achieve 20 % accuracy when applied to a sample that flows with a laminar flow. These results will be compared against experimental measurement, that will require the use of a low-pulsation pump. Indeed, any time dependence of the velocity would severely compromise the possibility to retrieve accurate diffusion information with spatially encoded diffusion NMR.

C. Convection flow

Convection is a heat transfer process in a fluid through the motion of matter, and happens due to temperature differences between two parts of the sample. In many PFG NMR experiments, the effect of convections translates into inaccurate estimates of the diffusion coefficients,⁵³ and this is also true for spatially encoded diffusion NMR. A typical convection velocity profile for an NMR tube is shown in . The difference between the density of heated and colder particles results into a complicated velocity distribution in the NMR tube. The possibility to compensate for this effect

in SPEN DNMR experiments is illustrated in Fig. 11, which shows the result of numerical simulation performed with a convection-compensated SPEN DSTE pulse (Fig. 1d).

The estimated diffusion coefficient, using Eq. 27 (which is equivalent to Eq. 34 with using $v_z = 0$), and no velocity correction during processing, is found to be $7.90(\pm 0.00) \times 10^{-10} \text{ m}^2/\text{s}$, when the data acquired during even echoes were processed. In contrast, with odd echo data the diffusion coefficient was found to be $8.94(\pm 0.05) \times 10^{-10} \text{ m}^2/\text{s}$. As in the case of constant and laminar flow, the even echo data provides more reliable results than the odd echo data. Further the diffusion coefficient is more accurate than the one obtained for the laminar flow. It is due to the fact that in convection, the effect of velocities throughout the sample gets compensated due to its anti-symmetrical distribution with respect to centre of the tube. In the case of laminar flow that the inability of performing the velocity effect correction results into the deviation from the accurate value of diffusion coefficient. In contrast, in the case of convection, although the same correction is not performed, compensation of error occurs between the effect of positive velocities in one half of the sample, and that of negative velocities in the other half.

Overall, these results explain why the convection compensated SPEN DNMR pulse sequence should have high accuracy in the case of convection flow, as was observed experimentally.

VI. CONCLUSIONS

In summary, we have provided a detailed description of flow effects in SPEN DNMR pulse sequences, through theoretical analyses and numerical simulations. These results explain the possibility to measure accurate diffusion coefficients with convection-compensated SPEN DNMR pulse sequences. They also give methods that should be applicable to systems in continuous flow, based on the processing of even-echo data only, and, in the case of plug flow, on a correction for sample motion effect. Overall, this work provides both physical insight and practical tools for applications of spatially encoded diffusion NMR methods in the presence of sample flow.

Author's contributions

RM, JND: conceptualisation, methodology, software, validation, formal analysis investigation, data curation, writing; RM: resources, visualisation; JND: supervision, project administration, funding acquisition.

ACKNOWLEDGEMENT

This work has received funding from the European Research Council (ERC) under the European Union's Horizon 2020 research and innovation program (grant agreement no 801774), the Region Pays de la Loire (Connect Talent HPNMR). The authors also acknowledge the French National Infrastructure for Metabolomics and Fluxomics MetaboHUB-ANR-11-INBS-0010 (www.metabohub.fr) and the Corsaire metabolomics core facility (Biogenouest).

DATA AVAILABILITY STATEMENT

The data that support the findings of this study are available from the corresponding author upon reasonable request.

REFERENCES

- ¹ G. Pagès, V. Gilard, R. Martino, and M. Malet-Martino, *Analyst* **142**, 3771 (2017).
- ² W. Li, H. Chung, C. Daeffler, J.A. Johnson, and R.H. Grubbs, *Macromolecules* **45**, 9595 (2012).
- ³ A. Chen, D. Wu, and C.S. Johnson, *J. Am. Chem. Soc.* **117**, 7965 (1995).
- ⁴ C. Barrère, M. Mazarin, R. Giordanengo, T.N.T. Phan, A. Thévand, S. Viel, and L. Charles, *Anal. Chem.* **81**, 8054 (2009).
- ⁵ F.M. Arrabal-Campos, P. Oña-Burgos, and I. Fernández, *Polym. Chem.* **7**, 4326 (2016).
- ⁶ Y. Cohen, L. Avram, and L. Frish, *Angew. Chemie - Int. Ed.* **44**, 520 (2005).
- ⁷ N. Giuseppone, J.L. Schmitt, L. Allouche, and J.M. Lehn, *Angew. Chemie - Int. Ed.* **47**, 2235 (2008).
- ⁸ L. Avram and Y. Cohen, *Chem. Soc. Rev.* **44**, 586 (2015).
- ⁹ J.H. Lamm, P. Niermeier, A. Mix, J. Chmiel, B. Neumann, H.G. Stammer, and N.W. Mitzel,

Angew. Chemie - Int. Ed. **53**, 7938 (2014).

¹⁰ R. Neufeld, T.L. Teuteberg, R. Herbst-Irmer, R.A. Mata, and D. Stalke, J. Am. Chem. Soc. **138**, 4796 (2016).

¹¹ G. Barozzino-Consiglio, G. Hamdoun, C. Fressigné, A. Harrison-Marchand, J. Maddaluno, and H. Oulyadi, Chem. - A Eur. J. **23**, 12475 (2017).

¹² S. Bachmann, B. Gernert, and D. Stalke, Chem. Commun. **52**, 12861 (2016).

¹³ D. Li, I. Keresztes, R. Hopson, and P.G. Williard, Acc. Chem. Res. **42**, 270 (2009).

¹⁴ S. Balayssac, S. Trefi, V. Gilard, M. Malet-Martino, R. Martino, and M.A. Delsuc, J. Pharm. Biomed. Anal. **50**, 602 (2009).

¹⁵ S. Trefi, V. Gilard, S. Balayssac, M. Malet-Martino, and R. Martino, Magn. Reson. Chem. **47**, (2009).

¹⁶ J.H. Vrijssen, I.A. Thomlinson, M.E. Levere, C.L. Lyall, M.G. Davidson, U. Hintermair, and T. Junkers, Polym. Chem. **11**, 3546 (2020).

¹⁷ A. Marchand, R. Mishra, A. Bernard, and J.-N. Dumez, Chem. – A Eur. J. (2022).

¹⁸ M.J. Thrippleton, N.M. Loening, and J. Keeler, Magn. Reson. Chem. **41**, 441 (2003).

¹⁹ L. Guduff, I. Kuprov, C. Van Heijenoort, and J.N. Dumez, Chem. Commun. **53**, 701 (2017).

²⁰ S. Ahola, V. V. Zhivonitko, O. Mankinen, G. Zhang, A.M. Kantola, H.Y. Chen, C. Hilty, I. V. Koptug, and V.V. Telkki, Nat. Commun. **6**, 1 (2015).

²¹ Y. Shrot and L. Frydman, J. Magn. Reson. **195**, 226 (2008).

²² G. Hamdoun, L. Guduff, C. Van Heijenoort, C. Bour, V. Gandon, and J.N. Dumez, Analyst **143**, 3458 (2018).

²³ V.V. Telkki, Magn. Reson. Chem. **56**, 619 (2018).

²⁴ L. Guduff, D. Kurzbach, C. van Heijenoort, D. Abergel, and J.N. Dumez, Chem. - A Eur. J. **23**, 16722 (2017).

- ²⁵ P.T. Callaghan and Y. Xia, *J. Magn. Reson.* **91**, 326 (1991).
- ²⁶ G.H. Sørland, J.G. Seland, J. Krane, and H.W. Anthonsen, *J. Magn. Reson.* **142**, 323 (2000).
- ²⁷ A. Jerschow and N. Müller, *J. Magn. Reson.* **125**, 372 (1997).
- ²⁸ H.Y. Carr and E.M. Purcell, *Phys. Rev.* **94**, 630 (1954).
- ²⁹ A.M.R. Hall, R. Broomfield-Tagg, M. Camilleri, D.R. Carbery, A. Codina, D.T.E. Whittaker, S. Coombes, J.P. Lowe, and U. Hintermair, *Chem. Commun.* **54**, 30 (2017).
- ³⁰ A. Caprihan and E. Fukushima, *Phys. Rep.* **198**, 195 (1990).
- ³¹ I. Swan, M. Reid, P.W.A. Howe, M.A. Connell, M. Nilsson, M.A. Moore, and G.A. Morris, *J. Magn. Reson.* **252**, 120 (2015).
- ³² A. Jerschow, *J. Magn. Reson.* **145**, 125 (2000).
- ³³ P. Callaghan, *Principles of Nuclear Magnetic Resonance Microscopy* (Clarendon Press, Oxford, 1993).
- ³⁴ E.M. Haacke, R.W. Brown, M.R. Thompson, and R. Venkatesan, *Magnetic Resonance Imaging Physical Principles and Sequence Design* (John Wiley & Sons, 1999).
- ³⁵ A. Saib, A. Bara-Estaún, O.J. Harper, D.B.G. Berry, I.A. Thomlinson, R. Broomfield-Tagg, J.P. Lowe, C.L. Lyall, and U. Hintermair, *React. Chem. Eng.* **6**, 1548 (2021).
- ³⁶ T.M. Barbosa, R. Rittner, C.F. Tormena, G.A. Morris, and M. Nilsson, *RSC Adv.* **6**, 95173 (2016).
- ³⁷ W.J. Goux, L.A. Verkruyse, and S.J. Saltert, *J. Magn. Reson.* **88**, 609 (1990).
- ³⁸ A. Jerschow and N. Müller, *J. Magn. Reson.* **132**, 13 (1998).
- ³⁹ T. Nishimura, M. Wakamatsu, and A.M. Morega, *Int. J. Heat Mass Transf.* **41**, 1601 (1998).
- ⁴⁰ and W.G.B. Victor Waluch, *J. Comput. Assisted Tomogr.* **8(4)**, 594 (1984).
- ⁴¹ A. Jerschow and N. Müller, *Macromolecules* **31**, 6573 (1998).
- ⁴² C.S. Johnson, *Prog. Nucl. Magn. Reson. Spectrosc.* **34**, 203 (1999).

- ⁴³ I.A. Thomlinson, M.G. Davidson, C.L. Lyall, J.P. Lowe, and U. Hintermair, *Chem. Commun.* **58**, 8242 (2022).
- ⁴⁴ C. Jacquemmoz, R. Mishra, L. Guduff, C. van Heijenoort, and J.N. Dumez, *Magn. Reson. Chem.* **60**, 121 (2022).
- ⁴⁵ I. Kuprov, *J. Magn. Reson.* **270**, 124 (2016).
- ⁴⁶ H.J. Hogben, M. Krzystyniak, G.T.P. Charnock, P.J. Hore, and I. Kuprov, *J. Magn. Reson.* **208**, 179 (2011).
- ⁴⁷ L. Guduff, A.J. Allami, C. Van Heijenoort, J.N. Dumez, and I. Kuprov, *Phys. Chem. Chem. Phys.* **19**, 17577 (2017).
- ⁴⁸ D. Sinnaeve, *Concepts Magn. Reson. Part A Bridg. Educ. Res.* **40 A**, 39 (2012).
- ⁴⁹ J.N. Dumez, *Prog. Nucl. Magn. Reson. Spectrosc.* **109**, 101 (2018).
- ⁵⁰ J. Valette, F. Lethimonnier, and V. Lebon, *J. Magn. Reson.* **205**, 255 (2010).
- ⁵¹ M. Nilsson, A.M. Gil, I. Delgadillo, and G.A. Morris, *Anal. Chem.* **76**, 5418 (2004).
- ⁵² M. Nilsson and G.A. Morris, *J. Magn. Reson.* **177**, 203 (2005).
- ⁵³ E. Martinez-viviente and P.S. Pregosin, **86**, 2364 (2003).
- ⁵⁴ I. Swan, *Advanced NMR Methods for Formulation Analysis*, The University of Manchester, 2015.

FIGURES

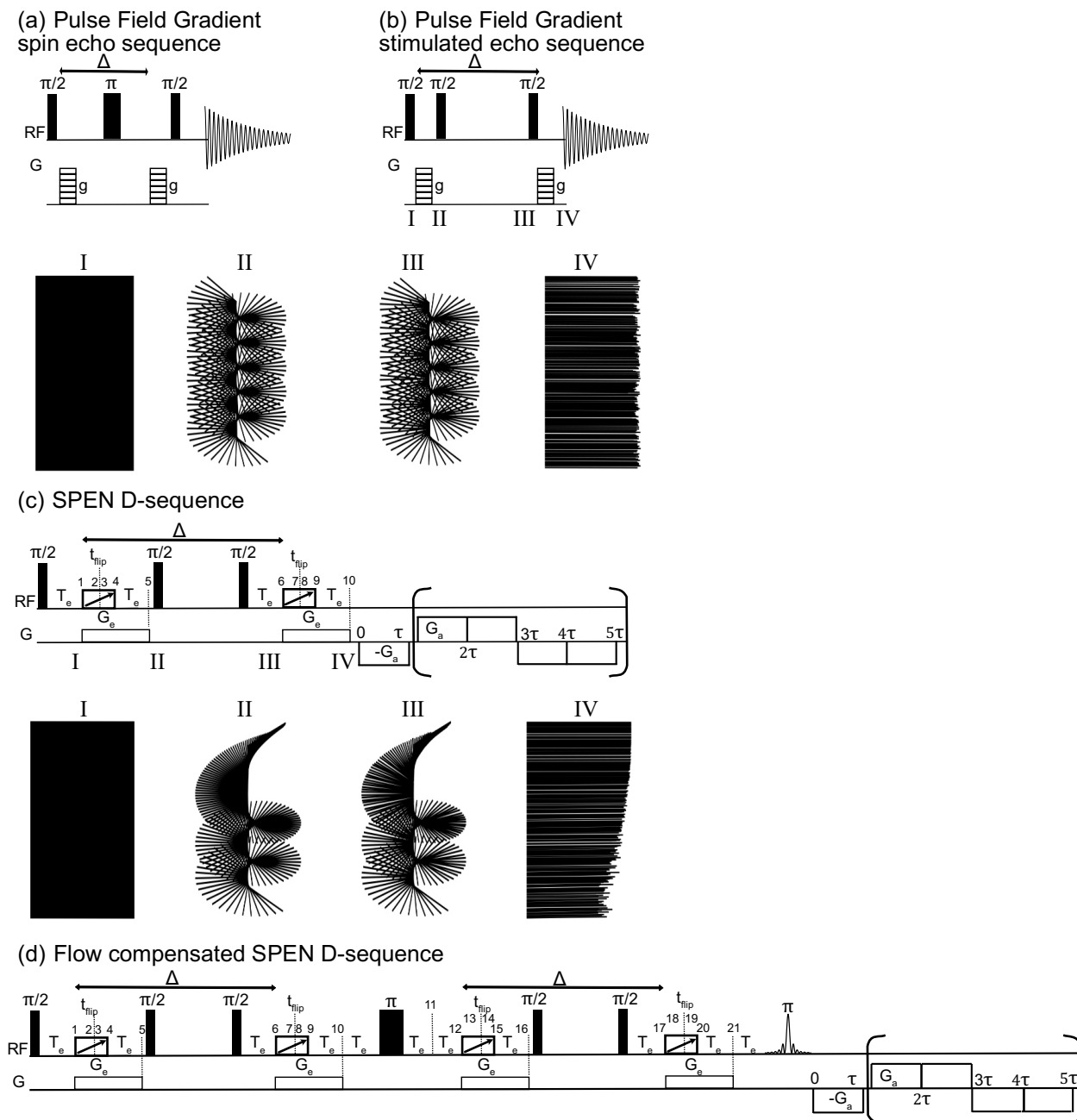


Fig. 1. Diffusion NMR pulses sequences. Hard RF pulses are shown as filled rectangles, swept RF pulses are shown as rectangles with an arrow, gradients pulses are represented as empty rectangles. The roman numbers (I, II, III, IV) in the bottom of (b) and (c) are used to show the helices at the corresponding positions of the pulse sequence. (a) Pulsed field gradient spin echo sequence. (b) Pulsed field gradient stimulated echo sequence. (c) Stimulated echo pulse sequence for spatially encoded diffusion-ordered NMR spectroscopy (SPEN DOSY STE). (d) Flow compensated double stimulated echo pulse sequence for spatially encoded diffusion-ordered NMR spectroscopy (SPEN DOSY DSTE). For sequence (b) and (c), the transverse magnetization as a function of axis- z is shown at specific stages of the sequence.

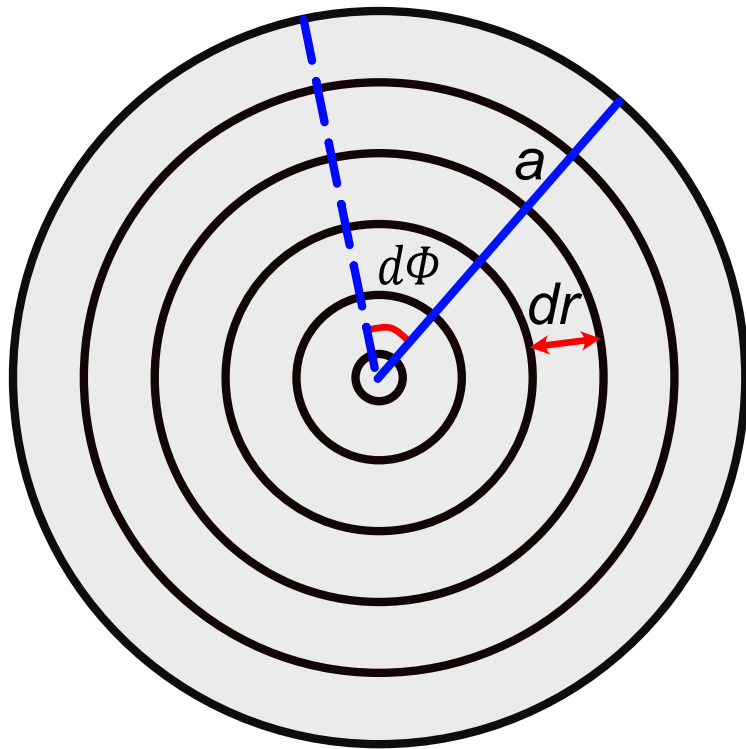


Fig. 2. Cross-section of an NMR tube representing the grids used for integration when simulating laminar and convection flow.

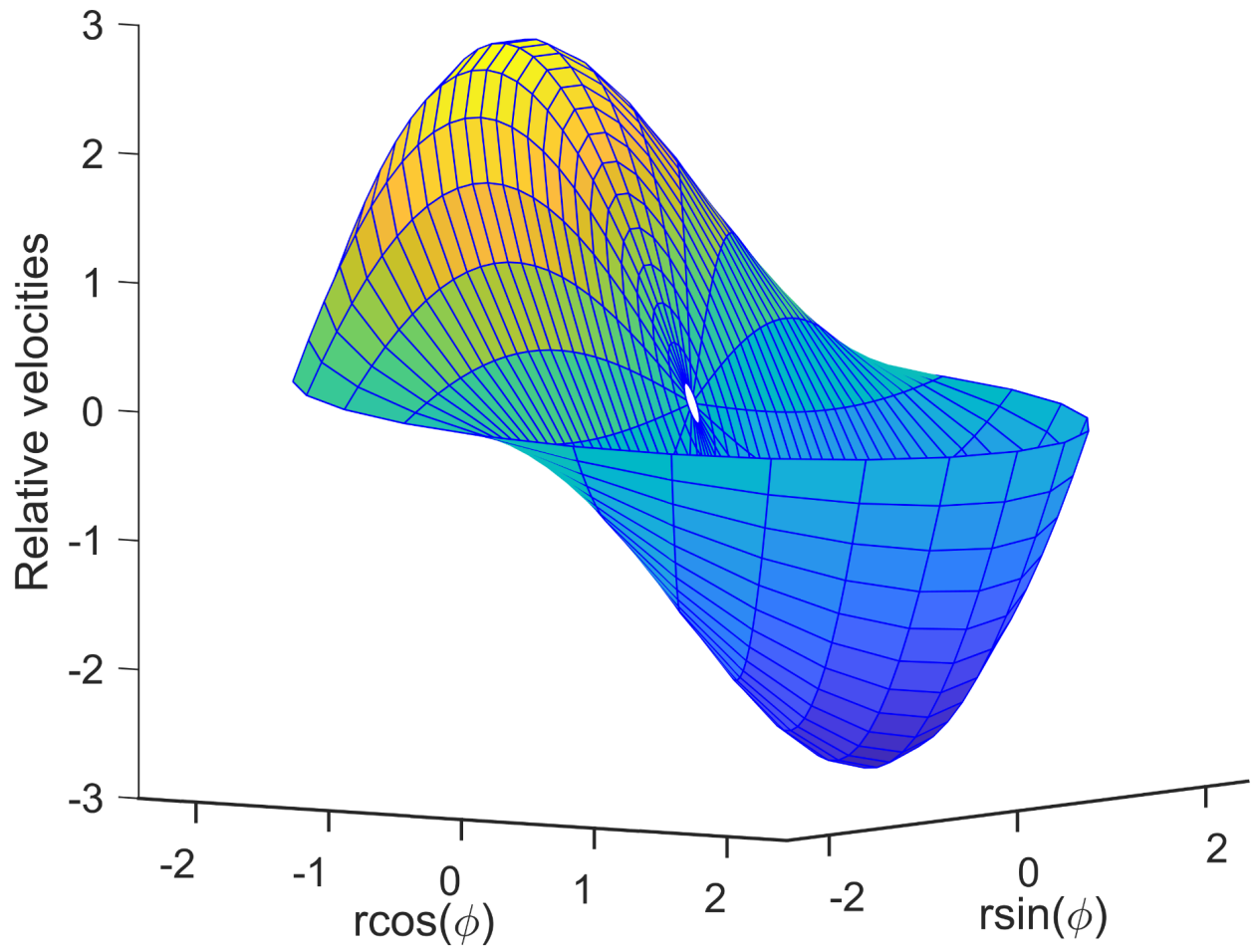


Fig. 3. Three-dimensional representation of convection velocity profiles in cylindrical coordinates. The velocities in left side of the tube are with positive sign while those in right are with negative sign. The vertical axis represents relative velocities of convection as a function of radial position.⁵⁴

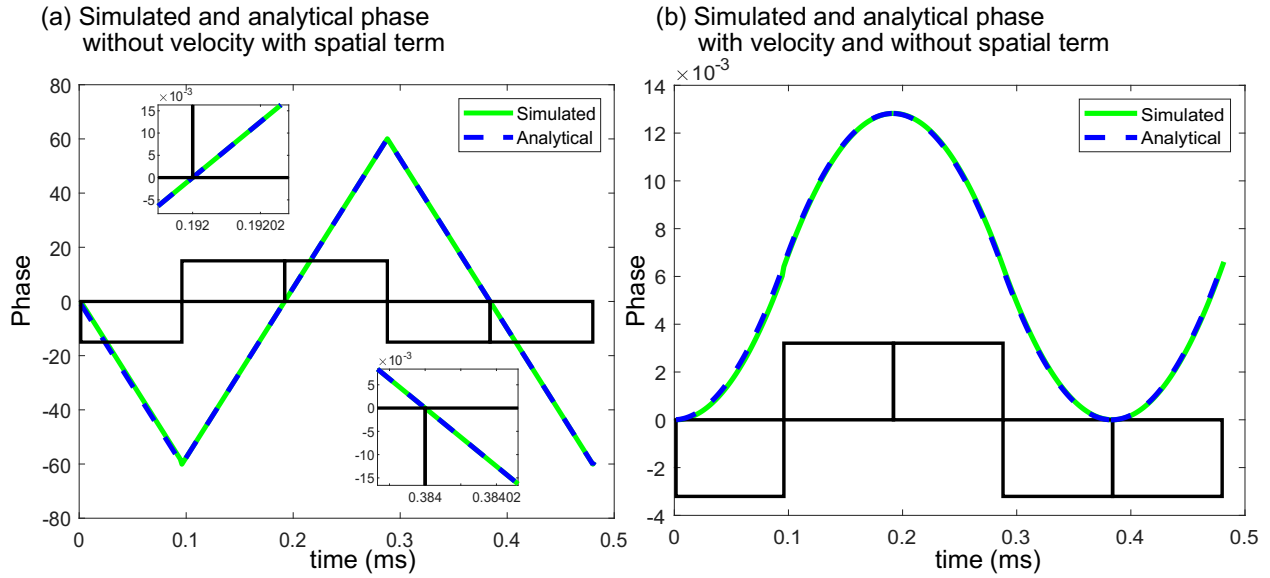


Fig. 4. Evolution of the phase of the magnetisation during EPSI. The rectangles represent acquisition gradients. The phase consists of two terms, i.e. the phase acquired due to spatial position (z) and the phase acquired due to velocity ($v_z t$). (a) On including the effect of both the terms, the comparison between simulated (solid-green) and analytical (dashed-blue) phases acquired by the magnetization at 4.5 mm with time. (b) On excluding the effect of spatial term, the comparison between simulated (solid-green) and analytical (dashed-blue) phases acquired by the magnetization with time. The phases in both the figures are getting refocused only at the middle of the even echo, not at the middle of the odd echo.

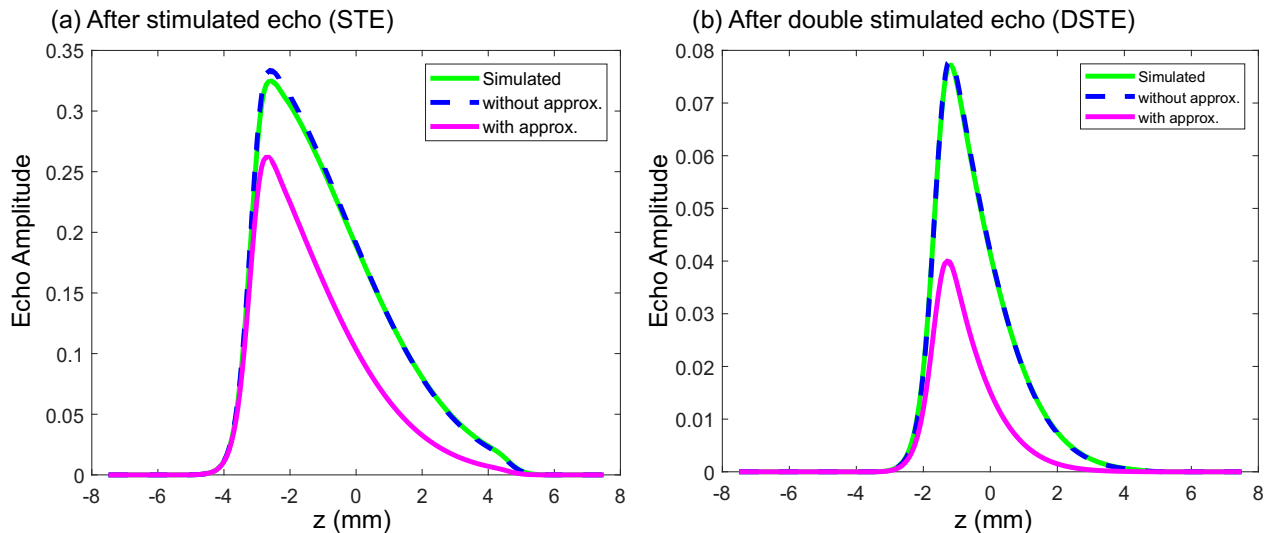


Fig. 5. Comparison between simulated and analytical echo amplitudes for the (a) SPEN STE and (b) SPEN DSTE pulse sequence, with constant velocity. Simulated echo amplitudes are shown in green. Analytical echo amplitudes obtained with the small displacement approximation for both diffusion and flow are shown in pink (Eq. 22 and 27. Analytical echo amplitudes obtained without the small displacement approximation for diffusion (Eq. 33 and Eq. 34) are shown in blue.

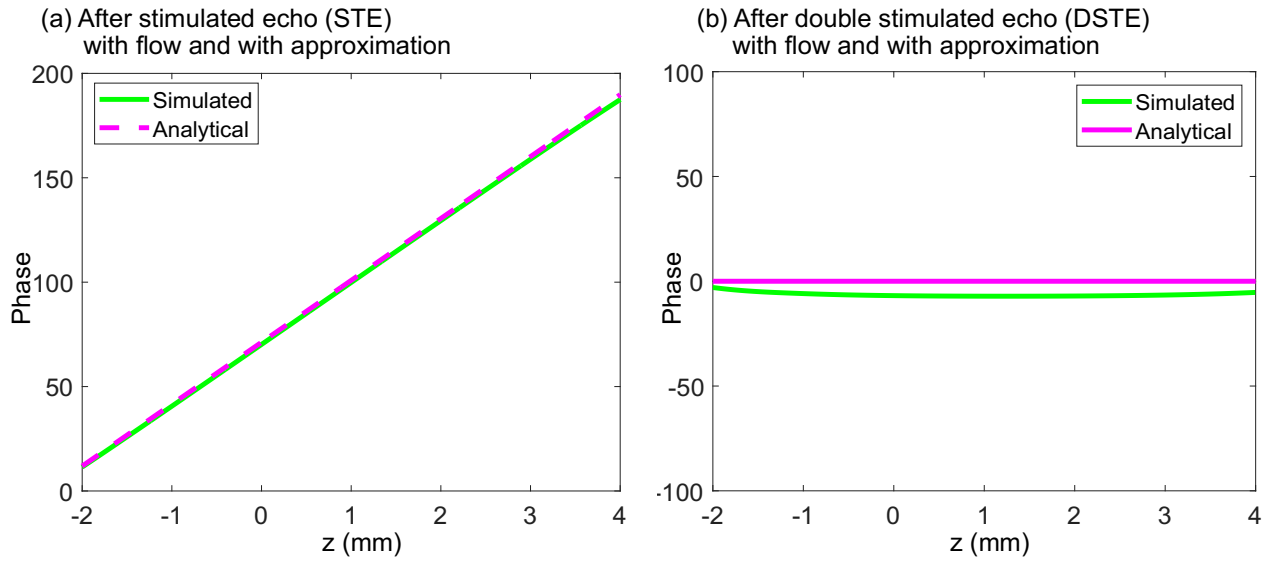


Fig. 6. Comparison between simulated and analytical phases for the (a) SPEN STE and (b) SPEN DSTE pulse sequence, with constant velocity. Simulated phases are shown in green. Analytical phases are shown in pink (Eq. 22 and 27).

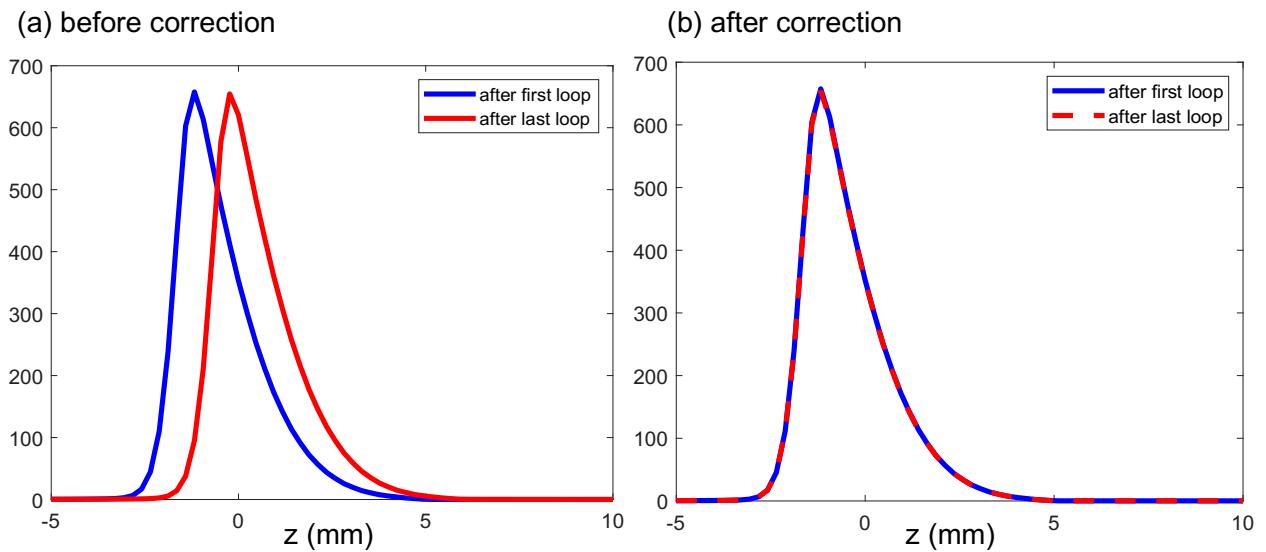
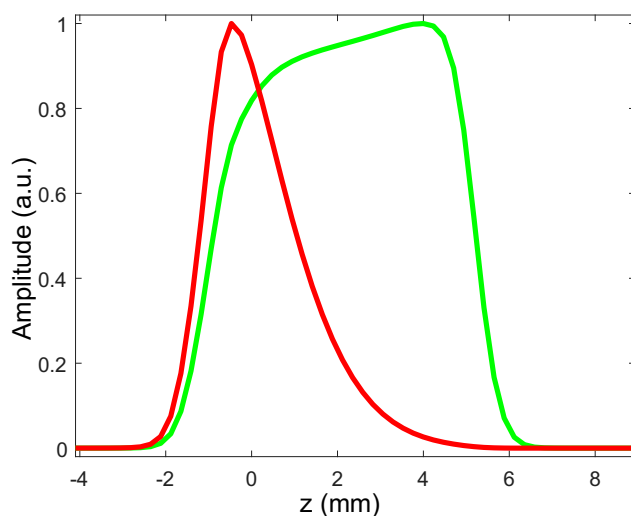


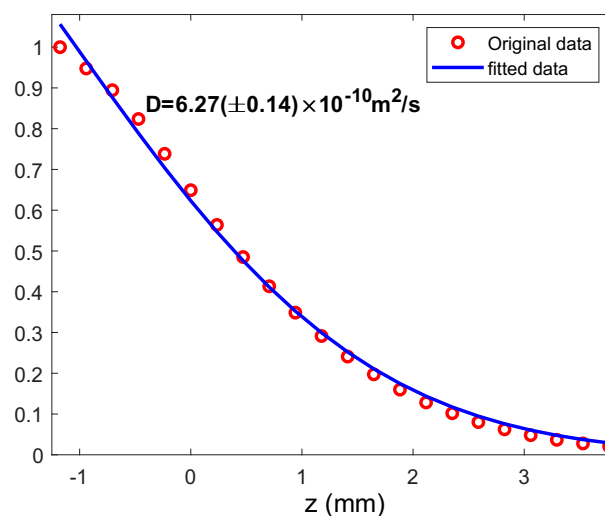
Fig. 7. Diffusion decay profiles (a) without and (b) with velocity correction after first ($n_l = 1$) and last EPSI loop ($n_l = 256$).

Without correction

(a) Diffusion decay curve and reference profile

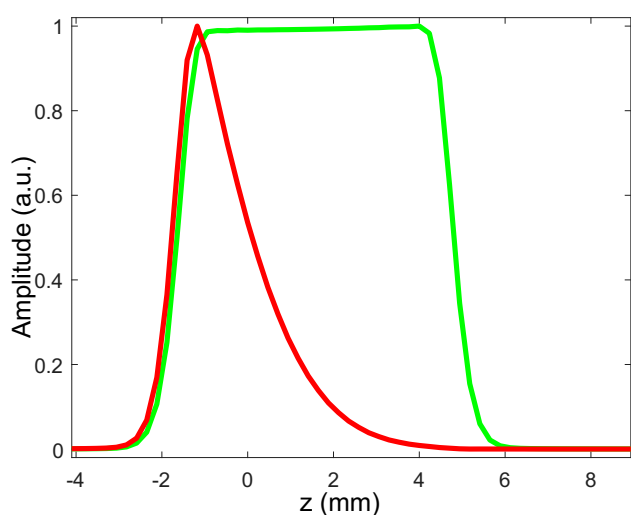


(b) Reference profile corrected diffusion data and fitted curve with Eq.34



With correction

(c) Diffusion decay curve and reference profile



(d) Reference profile corrected diffusion data and fitted curve with Eq.34

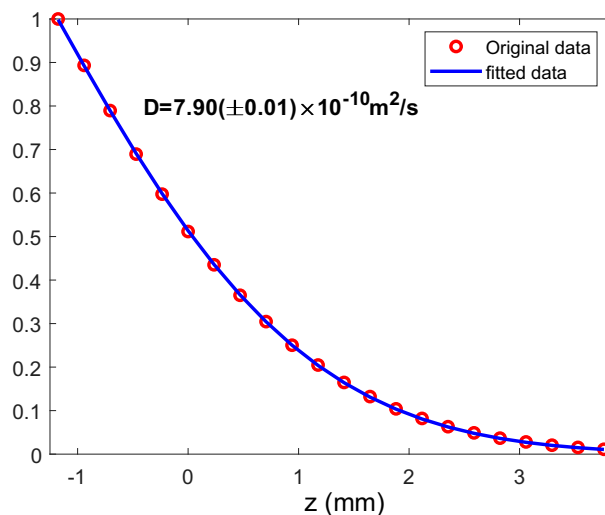


Fig. 8. Plug flow simulation. Diffusion decay profile (red) and reference profile (green) obtained (a) without and (c) with velocity correction during processing (Eq. 39). Diffusion decay data (red circle), obtained after dividing the diffusion decay profile by reference profile and fitted curve (blue line) (b) without and (d) with velocity correction during processing. Without correction the diffusion coefficient is found to be $6.27(\pm 0.14) \times 10^{-10} \text{ m}^2/\text{s}$, while after correction the value of diffusion coefficient is $7.90(\pm 0.01) \times 10^{-10} \text{ m}^2/\text{s}$.

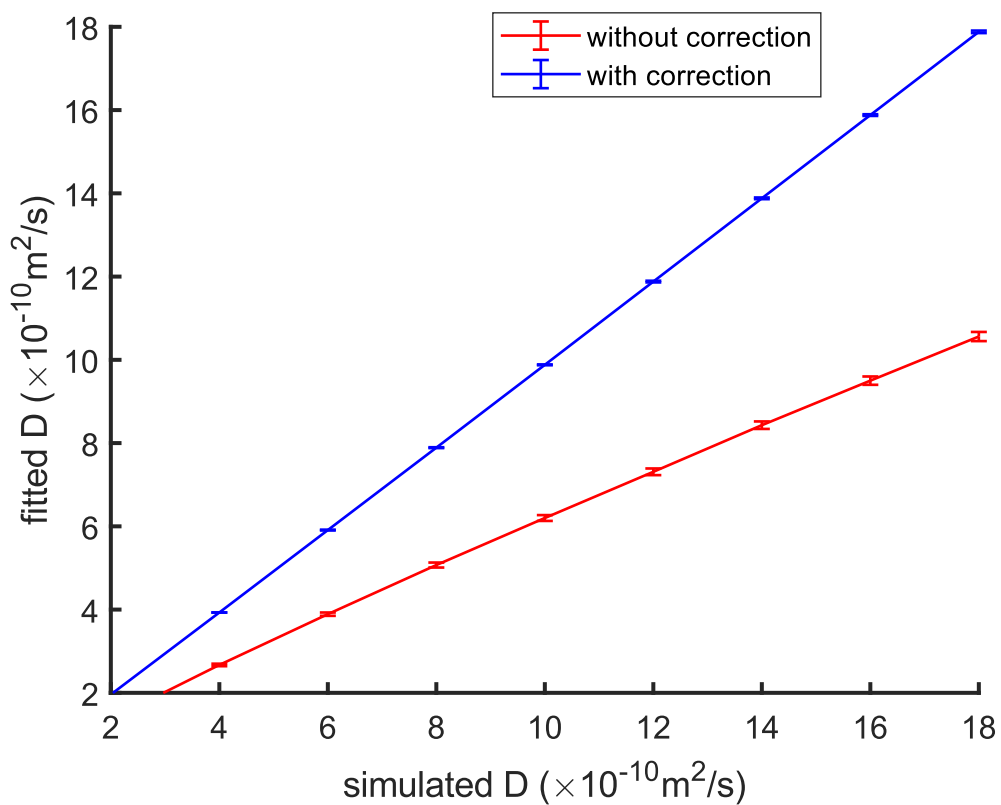
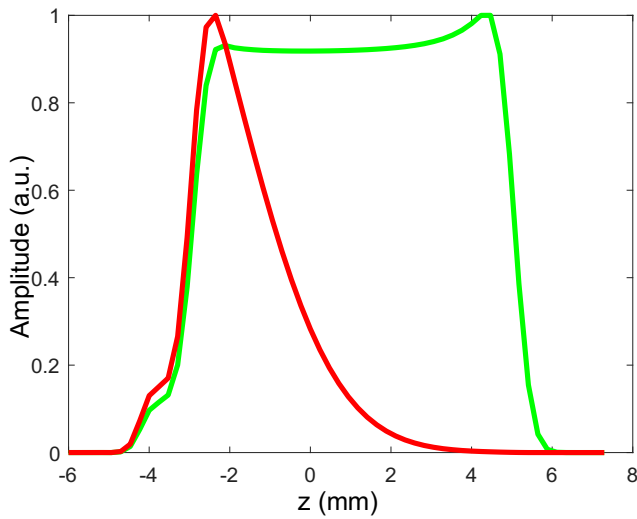


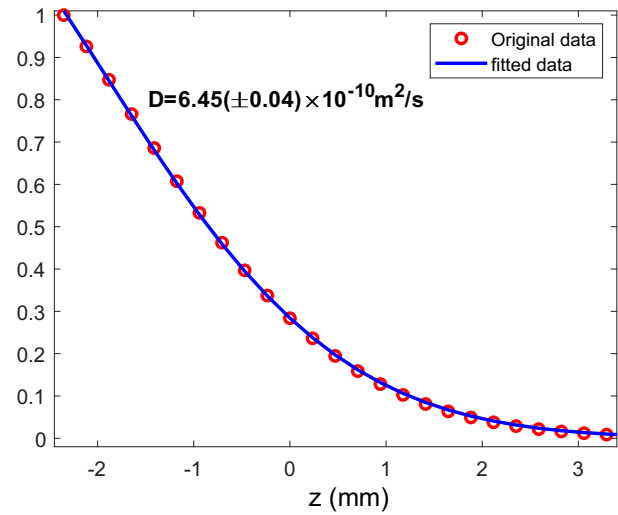
Fig. 9. Comparison between input and fitted values of the diffusion coefficient, for a series of values of the input diffusion coefficient. The analysis of the simulated data is carried out with (blue) and without (red) taking into account velocity effects.

Even echo processing

(a) Diffusion decay curve and reference profile

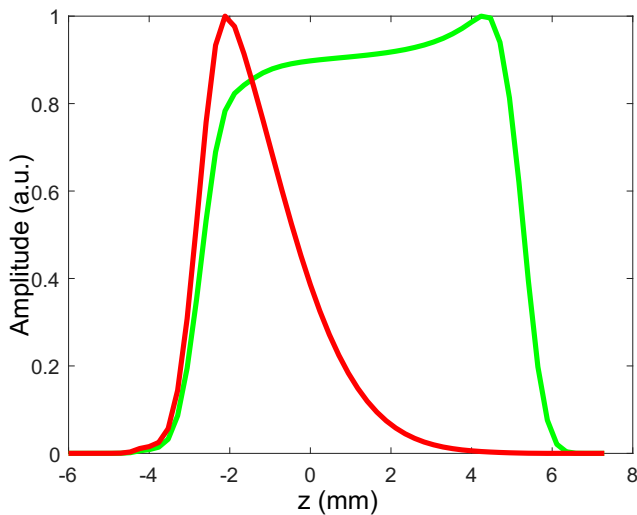


(b) Reference profile corrected diffusion data and fitted curve with Eq.34



Odd echo processing

(c) Diffusion decay curve and reference profile



(d) Reference profile corrected diffusion data and fitted curve with Eq.34

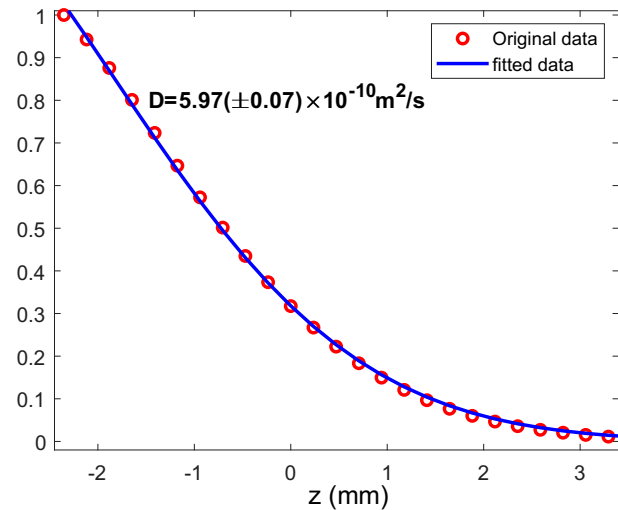
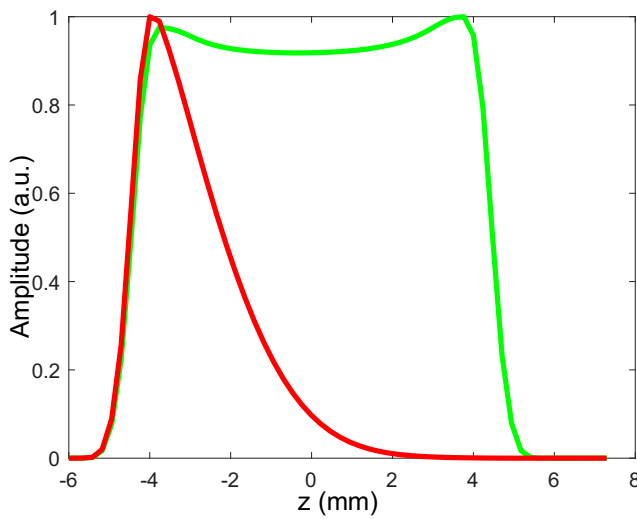


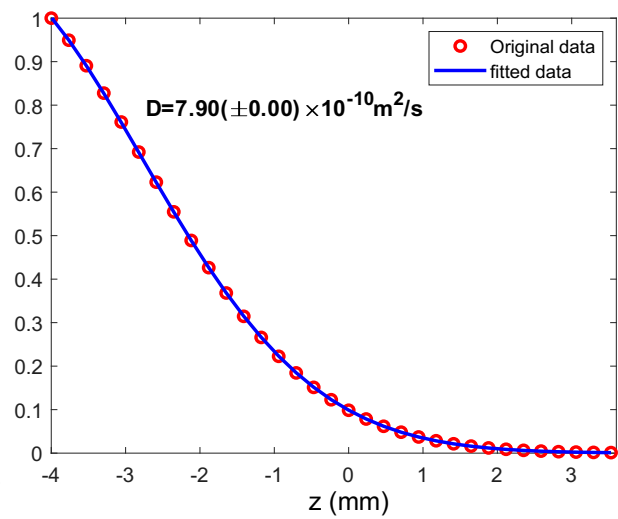
Fig. 10. Laminar flow simulation. Diffusion decay profile (red) and reference profile (green) obtained by processing and analysis of (a) even or (b) odd echoes of the EPSI train. Diffusion decay data (red circle), obtained after dividing the diffusion decay profile by reference profile and fitted curve (blue line) after processing and analysis of (a) even or (b) odd echoes of the EPSI train. Without correction the diffusion coefficient is found to be $6.45(\pm 0.04) \times 10^{-10} \text{ m}^2/\text{s}$, while after correction the value of diffusion coefficient is $5.97(\pm 0.07) \times 10^{-10} \text{ m}^2/\text{s}$.

Even echo processing

(a) Diffusion decay curve and reference profile

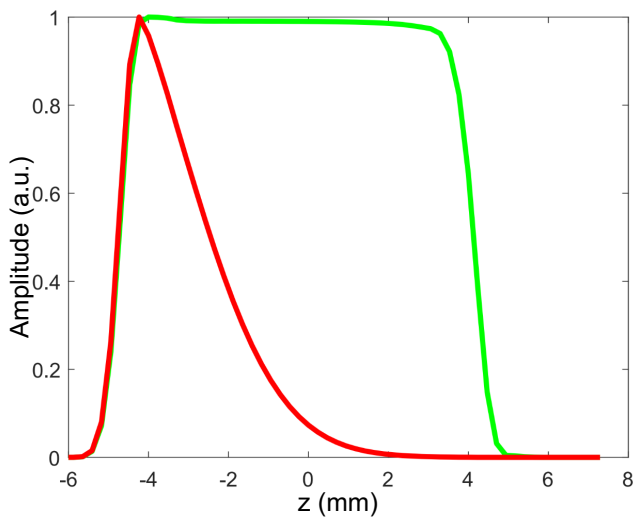


(b) Reference profile corrected diffusion data and fitted curve with Eq.34



Odd echo processing

(c) Diffusion decay curve and reference profile



(d) Reference profile corrected diffusion data and fitted curve with Eq.34

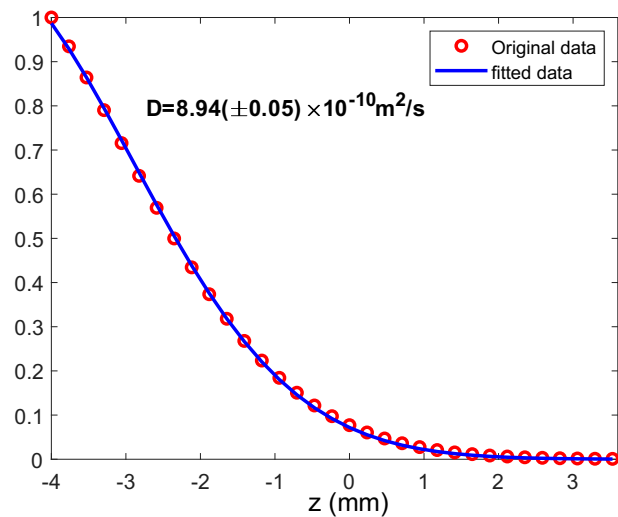


Fig. 11. Convection flow. Diffusion decay profile (red) and reference profile (green) obtained by processing and analysis of (a) even or (b) odd echoes of the EPSI train. Diffusion decay data (red circle), obtained after dividing the diffusion decay profile by reference profile and fitted curve (blue line) after processing and analysis of (a) even or (b) odd echoes of the EPSI train. Without correction the diffusion coefficient is found to be $7.90(\pm 0.00) \times 10^{-10} \text{ m}^2/\text{s}$, while after correction the value of diffusion coefficient is $8.94(\pm 0.05) \times 10^{-10} \text{ m}^2/\text{s}$.